Received: 27 June 2021 | Revised: 18 October 2021 | Accepted: 23 October 2021

DOI: 10.1002/mp.15327

RESEARCH ARTICLE

MEDICAL PHYSICS

Implementation and prospective clinical validation of AI-based planning and shimming techniques in cardiac MRI

Masoud Edalati[1] | **Yuan Zheng**[1] | **Mary P. Watkins**[2] | **Junjie Chen**[2] | **Liu Liu**[1] | **Shuheng Zhang**[1] | **Yanli Song**[1] | **Samira Soleymani**[3] | **Daniel J. Lenihan**[2] | **Gregory M. Lanza**[2]

[1] United Imaging Healthcare America, Inc., Houston, Texas, USA

[2] Cardiology Division, Washington University School of Medicine, St. Louis, Missouri, USA

[3] Department of Statistical and Actuarial Sciences, University of Western Ontario, London, Ontario, Canada

Correspondence
Gregory M. Lanza, Cardiology Division, Washington University School of Medicine, 4320 Forest Park Ave, St. Louis, MO 63108, USA.
Email: greg.lanza@mac.com

Funding information
NIH, Grant/Award Numbers: R01 CA216840-01A1, U54 CA199092

Abstract

Purpose: Cardiovascular magnetic resonance (CMR) is a vital diagnostic tool in the management of cardiovascular diseases. The advent of advanced CMR technologies combined with artificial intelligence (AI) has the potential to simplify imaging, reduce image acquisition time without compromising image quality (IQ), and improve magnetic field uniformity. Here, we aim to implement two AI-based deep learning techniques for automatic slice alignment and cardiac shimming and evaluate their performance in clinical cardiac magnetic resonance imaging (MRI).

Methods: Two deep neural networks were developed, trained, and validated on pre-acquired cardiac MRI datasets (>500 subjects) to achieve automatic slice planning and shimming (implemented in the scanner) for CMR. To examine the performance of our automated cardiac planning (EasyScan) and AI-based shim (AI shim), two prospective studies were performed subsequently. For the EasyScan validation, 10 healthy subjects underwent two identical CMR protocols: with manual cardiac planning and with AI-based EasyScan to assess protocol scan time difference and accuracy of cardiac plane prescriptions on a 1.5 T clinical MRI scanner. For the AI shim validation, a total of 20 subjects were recruited: 10 healthy and 10 cardio-oncology patients with referrals for a CMR examination. Cine images were obtained with standard cardiac volume shim and with AI shim to assess signal-to-noise ratio (SNR), contrast-to-noise ratio (CNR), overall IQ (sharpness and MR image degradation), ejection fraction (EF), and absolute wall thickening. A hybrid statistical method using of nonparametric (Wilcoxon) and parametric (*t*-test) assessments was employed for statistical analyses.

Results: CMR protocol with AI-based plane prescriptions, EasyScan, minimized operator dependence and reduced overall scanning time by over 2 min (~13 % faster, $p < 0.001$) compared to the protocol with manual cardiac planning. EasyScan plane prescriptions also demonstrated more accurate (less plane angulation errors from planes manually prescribed by a certified cardiac MRI technologist) cardiac planes than previously reported strategies. Additionally, AI shim resulted in improved B0 field homogeneity. Cine images obtained with AI shim revealed a significantly higher SNR (12.49%; $p = 0.002$) than those obtained with volume shim (volume shim: 32.90 ± 7.42 vs. AI shim: 37.01 ± 8.87) for the left ventricle (LV) myocardium. LV myocardium CNR was 12.48% higher

for cine imaging with AI shim (149.02 ± 39.15) than volume shim (132.49 ± 33.94). Images obtained with AI shim resulted in sharper images than those obtained with volume shim ($p = 0.012$). The LVEF and absolute wall thickening also showed that differences exist between the two shimming methods. The LVEF by AI shim was shown to be slightly larger than LVEF by volume shim in two groups: 2.87% higher with AI shim for the healthy group and 1.70% higher with AI shim for the patient group. The LV absolute wall thickening (in mm) also showed that differences exist between shimming methods for each group with larger changes observed in the patient group (healthy: 3.31%, $p = 0.234$ and patient group: 7.29%, $p = 0.059$).

Conclusions: CMR exams using EasyScan for cardiac planning demonstrated accelerated cardiac exam compared to the CMR protocol with manual cardiac planning. Improved and more uniform B0 magnetic field homogeneity also achieved using AI shim technique compared to volume shimming.

KEYWORDS
AI-based cardiac planning, AI-based cardiac shim, artificial intelligence

1 | INTRODUCTION

Cardiovascular magnetic resonance (CMR) is a noninvasive imaging technique that is considered the gold standard for the assessment of cardiac structure and function.[1,2] CMR provides prognostic evidence, changes patient management, reduces the need for other tests, and is supported by European and US consensus panel reports.[1,3,4] While the power of CMR is unquestioned, implementation of the complex technique requires specialized technologist training, skills, and experience. Moreover, patient throughput for fully implemented data acquisitions with extensive myocardial characterization are slow, challenging patient tolerance and requirements to limit physical motion, comply with repeated breath hold requests, and to lie flat in situations that may be claustrophobic or uncomfortable. Reaching the ambitious goals of this program requires integrating a series of improvements that shorten and simplify workflow, preserve image quality (IQ), enhance study-to-study uniformity, and greater patient compliance ease.

A successful CMR scan depends on accurate slice geometry prescription, which conventionally requires several scout scans with breath-holding and manual adjustment of the scan planes by a technologist, adding additional scan time, patient discomfort, and workflow complexity. Avoidable delays due to increased image acquisition times, such as prolonged image planning or repeat breath-holds decrease patient procedural tolerance and lower case throughput. Previous CMR studies have reported geometry prescription processes using automatic or semi-automatic slice alignment methods.[5–12] Lelieveldt et al.[5,6] matched the scout images to thoracic anatomy models and estimated the left ventricle (LV) orientation for automatic view planning; however, it could be used only for short-axis slice alignment, and the computational time took 3–5 min. Jackson et al.[7] segmented blood pool using expectation maximization algorithm, which is a semi-automatic approach where only the LV long axis can be determined. Dwivedi et al.[8] and Darrow et al.[9,10] presented an anatomy-guided methods that require extra imaging to determine the orientation of the LV. Both Lu et al. and Nitta et al.[11,12] employed machine learning techniques to detect a few predefined cardiac landmarks that each reference plane has to pass through so these planes can be positioned. However, these methods are sensitive to the errors of the detected landmarks and subject to absence of landmarks in the volume. Most importantly, the optimal position of the reference planes differs from person to person and is found not necessarily passing through those predefined landmarks. We propose a new automatic slice alignment method (EasyScan) based on deep learning regression network. Instead of relying on a few anatomical points, the plane is determined using all voxels in the neighborhood, which are more robust against inevitable landmark detection errors and clear the ambiguity of landmark annotation.

In CMR imaging, subject-induced magnetic field inhomogeneities can be pronounced due to susceptibility changes within the field of view (FOV).[13] Tissue-air boundaries compromise the B0 field, and careful shimming is required to establish a homogeneous and on-resonance B0 field around the heart. This is particularly true when a balanced steady state free precession (bSSFP) sequence is used for acquisition, which is sensitive to off-resonance effect.[14] In general, a "frequency-scout" is involved in the workflow, which collects a series of images with different off-resonance frequencies to help the operator find the best scanner frequency. Unfortunately, this process is both time-consuming and operator dependent. To address these issues, a generalized shimming tool using a mask-based artificial intelligence (AI) segmentation technique (AI shim) was developed

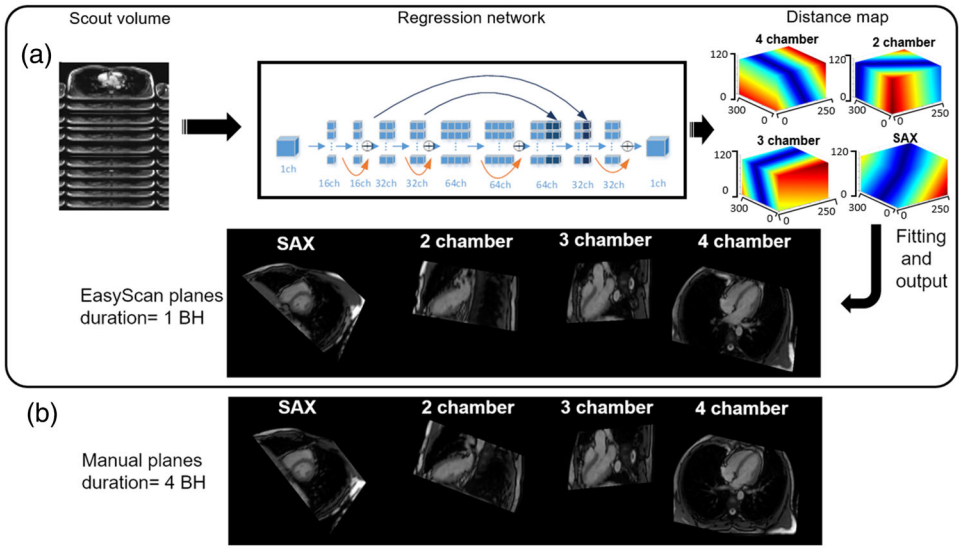

FIGURE 1 An overview of EasyScan workflow for cardiac planes prescription (a). The regression network consists of a chain of convolutional layers: convolutional layer with kernel size of $3 \times 3 \times 3$ voxels (light blue arrow), convolutional layer with kernel size of $5 \times 5 \times 5$ voxels combined with sum (orange arrow), the dark blue arrow forward the features extracted from early stage to the right part of the convolutional neural network (CNN). The output of the EasyScan obtained from a volunteer (a single breath-hold duration) is also illustrated. An example of cardiac planes (short-axis (SAX), two, three, and four-chambers) manually obtained (immediately after EasyScan) with four breath-holds (of the same volunteer) is shown (b)

for CMR scans. Briefly, a stack of transverse slices is acquired at the beginning of the study to establish the shimming currents, which automatically adjust the field for subsequent cardiac scans.

In this study, implementation of in-line AI-based cardiac planning and shimming are evaluated as initial tools to reduce technical complexity and time for execution as a means to achieve improved patient exam compliance.

2 | MATERIALS AND METHODS

2.1 | Implementation of AI-based cardiac planning

The AI-based cardiac planning (EasyScan) algorithm (Figure 1a) consists of three steps: (1) segment heart regions using the Otsu method, (2) calculate distance map using trained regression network, and (3) fit the plane using least square method. To reduce the computational time and improve method efficiency, the heart regions were segmented using the Otsu method, and a binary mask was generated. Around the gravity centroid of the binary segmentation mask, the cardiac region of interest (ROI) was cropped to the size of $120 \times 120 \times 120$ mm^3, which can cover great majority of volunteers, and resampled to an isotropic voxel spacing of 3.9 mm^3, which balances the computation speed and accuracy. To determine the spatial position of a cardiac plane, a distance map to the plane was calculated (see Supplementary Material for EasyScan) using a regression network, which contained a chain of approximate symmetrical convolutional layers. In Figure 1a, the light blue arrow shows the combination of convolution layer that uses a volumetric kernel size of $3 \times 3 \times 3$ voxels and a rectification layer (except for the last one), which has a convolution layer with a volumetric kernel of $5 \times 5 \times 5$ voxels and no rectification layer. The orange arrow indicates a convolution layer with a volumetric kernel of $5 \times 5 \times 5$ voxels (combined with sum). The layers within the red box consist of a residual function similar to the approach presented in Milletari et al.[15] The dark blue arrow forwards the features extracted from early stages of the left part of the convolutional neural network to the right part.[16] Each convolution layer is followed by a batch norm layer applied with appropriate padding. The batch norm layer, the residual blocks, and the connection layers improved the convergence time and accuracy of the model. No down- or up-sampling was used. The loss function applied in the training procedure was the L1 norm between the output of the network and the ground truth distance map (using multiplanar reconstruction images; see Supplementary Material for EasyScan). Finally, the plane of interest was calculated by a least square fitting method with a distance threshold (0.05). Coordinates with pixel values higher than the threshold were excluded to avoid excessive influence on the distance estimate by pixels far from the desired plane. To train the EasyScan network, 2D multi-slice images were pre-acquired with electrocardiography (ECG)-gated bSSFP during a single BH. EasyScan acquisition parameters were as

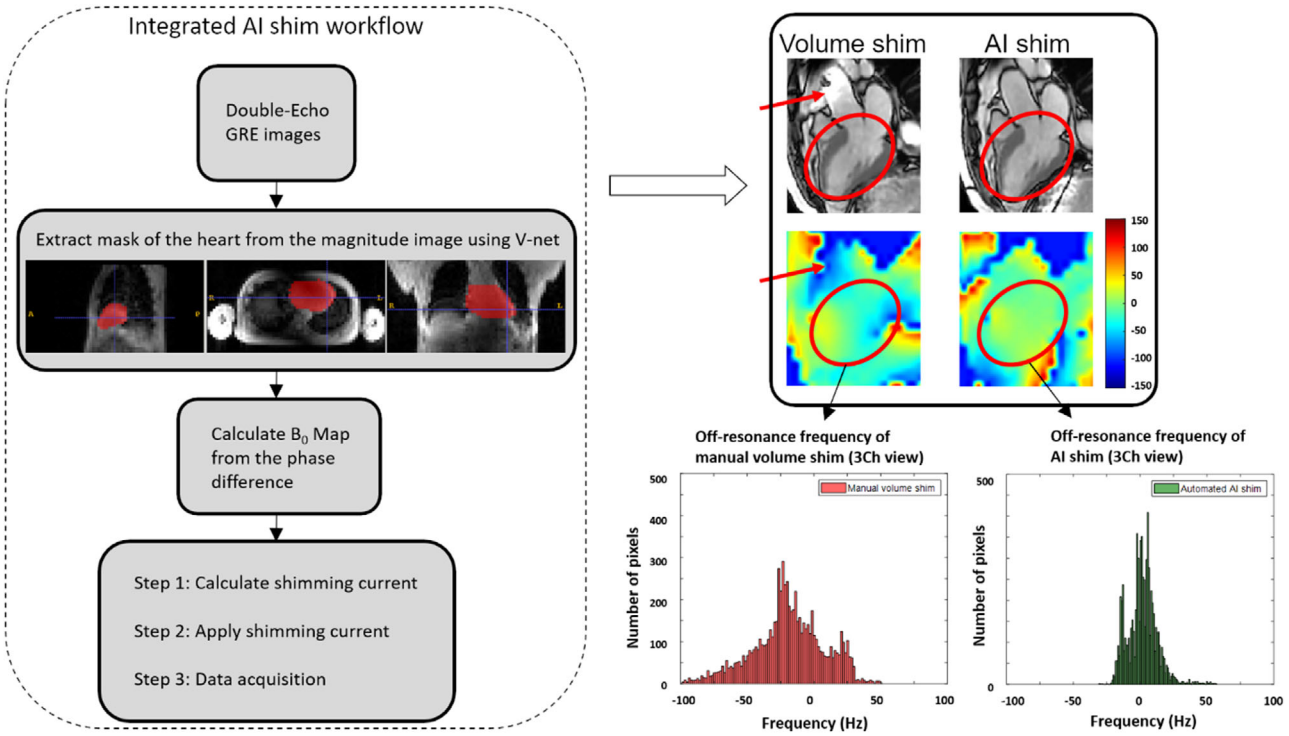

FIGURE 2 Schematic representation of automated artificial intelligence (AI) shim procedure using image segmentation neural network with V-net structure. Single-slice three-chamber cine images and B0 field maps of a volunteer acquired with each of two shimming procedures (manual volume shim and AI shim) show a more uniform field distributions resulted from AI shimming. Off-resonance frequency (Hz) histograms of heart regions (red circle) obtained from volume shim and AI shim are also illustrated

follows: TR/TE = 3.0/1.5 ms, matrix = 192 × 164 ~ 384 × 328, spatial solution = 1.1–2.5 × 1.1–2.5 mm^2, number of slices = 20, slice thickness = 7 mm (no gap), flip angle = 85, and one slice per R-R interval. The scanning time was set to <20 s. Images from 255 healthy volunteers (men and women, 22–60 years) were used for network training in addition to images collected with manual slice positioning for comparisons. The network was deployed in-line and on an NVIDIA GeForce GTX 1080 GPU with 12 GB memory generating slice prescriptions in real time (0.2 s). The network was tested on 57 subjects, and less than 2% of the output slices required further adjustment by radiologists.[17]

2.2 | Implementation of AI-based cardiac shimming

AI-based cardiac shim (AI shim) uses a dual echo 3D gradient echo sequence with breath-hold to collect the 3D anatomical structure and B0 field map of cardiac regions (Figure 2). The heart and non-heart regions were separated using an image segmentation neural network with a V-net structure.[15] Inputs of the network were transverse images covering the whole heart; outputs were masks of the heart. The network was trained on data from 400 volunteers with 3D scans with isotropic 6.7 mm^3 resolution and 48 × 48 × 32 image volume patch. The heart volumes of interests were manually delineated as the output for training. Focal loss and dice factor were used for network training and evaluation. For the V-net loss function, the focal loss was applied as a modulating term to the cross entropy loss to resolve the class imbalance and classification problems. The network was deployed on an NVIDIA GeForce GTX 1080 GPU with 12 GB memory and allowed real-time mask extraction (<1 s). The segmentation accuracy was validated on 98 testing subjects with a dice factor > 0.92. With the AI-segmented cardiac mask and B0 field map, the shimming currents were determined separately for each application with different weights for the in-mask and out-of-mask FOV via standard spherical harmonics analysis (see Supplementary Material for AI shim). The shimming currents were solely calculated to optimize the field of the heart for cardiac cine, while the out-of-mask FOV was employed for dark-blood imaging, allowing better subcutaneous fat saturation.

2.3 | Study population for clinical validation

This pilot study was approved by the institution's human subjects review committee. For EasyScan validation,

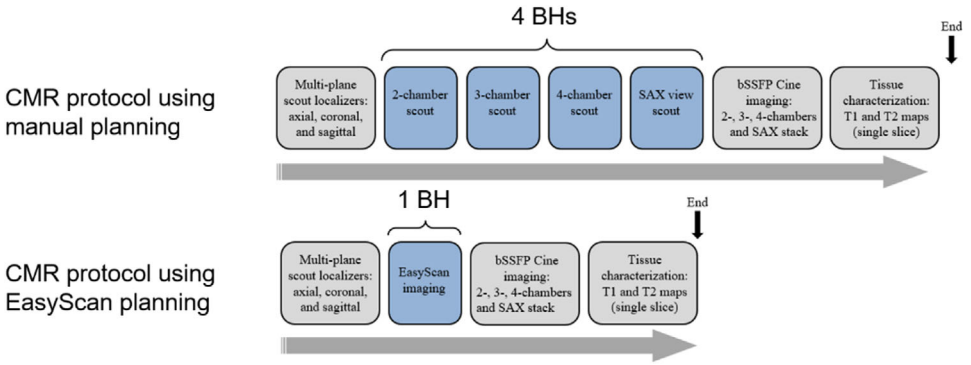

FIGURE 3 Illustration of the study protocols: Cardiovascular magnetic resonance (CMR) protocol using manual cardiac planning (duration: four breath-holds (BHs)) and the same CMR protocol but with automated EasyScan planning (duration: 1 BH)

10 healthy volunteers were enrolled and scanned twice on the same day using two identical standard CMR protocols[18]: (1) with manual cardiac planning and (2) with automated EasyScan (Figure 3). To minimize MRI scan bias, half of the subjects were initially scanned with the protocol using EasyScan followed by protocol using manual cardiac planning, and half were scanned in the reversed order. Subsequently, to compare the performance of AI shim with cardiac volume shim, 20 subjects: 10 healthy volunteers (five females and five males, ages 23–80 years) and 10 cancer patients (five females and five males, ages 24–71 years) referred for CMR were studied under informed consents. All subjects recruited for study participation met the study enrollment inclusion/exclusion criteria prior to enrollment. Their demographic characteristics including mean (± standard deviation [SD]) age, height, weight, body mass index, heart rate, cancer type, and their oncology history duration are presented in Table 1.

TABLE 1 Population characteristics

	Healthy ($n = 10$)	Patients ($n = 10$)	*p value*
Age (years)	52.60 ± 21.20	47.60 ± 13.65	0.559
Height (m)	1.73 ± 0.09	1.70 ± 0.09	0.533
Weight (Kg)	78.20 ± 14.44	80.29 ± 13.46	0.755
BMI (Kg/m^2)	25.95 ± 3.72	27.83 ± 5.53	0.408
Heart rate (bpm)	65.10 ± 8.55	74.00 ± 11.88	0.018
Gender			
Female	5	5	NA
Male	5	5	NA
Cancer types			
Breast cancer	NA	4	NA
Sarcoma cancer	NA	3	NA
Lymphoma cancer	NA	1	NA
Leukemia cancer	NA	1	NA
Myeloma cancer	NA	1	NA
Oncology history duration (years)	NA	11.00 ± 8.53	NA

Note: Age, height, weight, body mass index (BMI), heart rate, and patient's oncology history are represented as mean ± standard deviation. Statistical significance level was set at $p < 0.05$.

2.4 | MRI acquisition for clinical validation

CMR scans were performed on a wide bore 1.5 T clinical MRI scanner (uMR570; United Imaging Healthcare, Shanghai, China) with maximum gradient strength of 45 mT/m (maximum slew rate of 200T/m/s). All subjects were scanned in the supine position (head-first) using a 12-channel body array coil. The MRI sliding table and subjects were maintained (head-first and supine position) at the magnet isocenter with no positional offset between two CMR imaging protocols. For EasyScan, the two protocols shared identical scans with the exception that the standard scout scans (four breath-holds) were replaced with a single EasyScan (one breath-hold) as shown in Figure 3. For cine images (two-, three-, four-chambers and short-axis stack views) using the protocol with manual cardiac planning, a multi-plane scout was acquired in transverse, coronal, and sagittal views followed by single slice scout images for all four views (requiring four breath-holds). Short-axis stack cine slices were planned parallel to the mitral valve at the LV base with additional slices covering the entire heart to the apex (~10–12 slices with no interslice gap). In contradistinction to manual planning, the automated EasyScan planning acquired all views needed to plan for cine images in one breath-hold, obviating the need for manual cardiac planes adjustments. Single slice (two-, three-, four-chambers) and multi slice SAX cines were acquired using a segmented bSSFP sequence with retrospective ECG gating in a breath-hold fashion (1 slice, ~7–10 s) with at least 15–20 s rest period between breath-holds for SAX cine imaging. The following acquisition parameters were used for cine imaging:

TR/TE = 2.98/1.4 ms, slice thickness of 8 mm, rectangular FOV 360 × 320 mm^2, pixel size 1.9 × 1.6 mm^2, acceleration factor 2, flip angle 80°, bandwidth 1000 Hz, and 25 reconstructed phases. Cardiac cine of 2, 3, 4 chambers and short axis views were used for the comparison between manual volume shim and AI shim. When manually placing the volume shim box for CMR, multiple planes were utilized. In the transverse plane, the shim was placed over the heart to include descending aorta with sagittal and coronal planes to verify placement.

2.5 | Image analysis for clinical validation

The stack of cine SAX images was processed inline with an automated cardiac post-processing tool available on the scanner to derive ejection fraction (EF) and absolute LV wall thickening (defined as end-systolic [ES] minus end-diastolic [ED] wall thickness). Prior to any calculation, all SAX cine images were automatically segmented and registered followed by motion correction. The remaining cine images were exported for offline post-processing to calculate signal-to-noise ratio (SNR), contrast-to-noise ratio (CNR), and image sharpness for four different views: two-, three-, four-chambers, and SAX. SNR was computed with a previously described method under the assumption that noise has a Rayleigh distribution.[19] The LV and right ventricle (RV) SNRs were measured using ROI within LV and RV at ED phase for all slices. However, RV SNR and CNR were only measured using the four-chamber and SAX views. ROIs were drawn manually for myocardium and blood pool cavity, excluding boundaries to minimize partial volume effects. CNR was calculated as the difference between LV/RV and blood pool SNRs. Image sharpness (inverse of the blur quality index) was estimated using a no-reference perceptual blur metric ranging from 0 to 1, that is, worst to the best quality, respectively, in terms of image sharpness.[20,21] Image sharpness was then measured for each cine image averaged over all phases for each cardiac view. The subjective assessment of bSSFP cine images for LV and RV was based on the SAX images acquired with volume shim and AI shim. A five-point rank score was applied by two blinded, independent MRI experts (with more than 10 years' experience each in CMR imaging) who evaluated MR image degradation, including wrap-around, respiration bulk motion, cardiac ghosts, flow artifact, shim artifact, noisy images, and image blurring for SAX stack. The IQ was scored as: 5 = excellent IQ without noticeable artifact; 4 = above average IQ with mild artifact/mildly impacting analysis; 3 = adequate IQ with moderate artifact/moderately impacting analysis, but trustable; 2 = suboptimal IQ with marked artifact, but not all structures; 1 = poor IQ with severe artifact, non-diagnostic.

2.6 | Statistical analysis for clinical validation

The measured parameters consisted of (1) total scan time and cardiac plane angulation accuracy for automated EasyScan, (2) SNR, CNR, image sharpness, EF, and LV absolute wall thickening from images obtained with volume shim and AI shim. To assess statistical differences, a hybrid method using nonparametric and parametric statistical assessments was applied. The statistical significance level was set at $p < 0.05$ for all analyses. Data distributions were tested for normality with the Shapiro Wilk W test. To assess AI shim performance, the difference between two levels, the volume shim and AI shim, was determined for the LV and RV two-, three-, four-chambers, and SAX views. If the differences were normally distributed, the paired *t*-test was used to assess statistical significance. For non-normally distributed data, the Wilcoxon signed rank test was used. Means, SD, and 95 % confidence intervals were used for descriptive statistics. Statistical analyses were performed with R statistical software (version 4.0.2; R Core Team 2020).

3 | RESULTS

3.1 | Subject characteristics

CMR scans were successfully performed on all recruited subjects with sufficient IQ as visually inspected and reviewed by a certified MRI technologist. The subjects' characteristics are summarized in Table 1 with the mean age (year) of 52.60 ± 21.20 and 47.60 ± 13.65 for the healthy and cardio-oncology patients, respectively. In addition, the mean heart rate (bpm) of the cardio-oncology patients was higher than that of the healthy subjects (74.00 ± 11.88 for patients vs. 65.10 ± 8.55 for healthy, $p < 0.05$).

3.2 | Manual cardiac planning versus AI-based EasyScan planning

3.2.1 | CMR protocol scan time with EasyScan

The scan time for single slice retrospective cine imaging (1 BH for each of two-, three-, and four-chamber views) was approximately 7–10 s, while the scan time of the SAX stack cine was ~205–235 s for 10 slices with a rest period of 15–20 s after each breath-hold. EasyScan mean cardiac protocol scan times (extracted from Dicom header timestamp) for 10 subjects were 19.26 ± 0.77 min versus 16.70 ± 0.86 min for the standard CMR protocol with manual cardiac planning

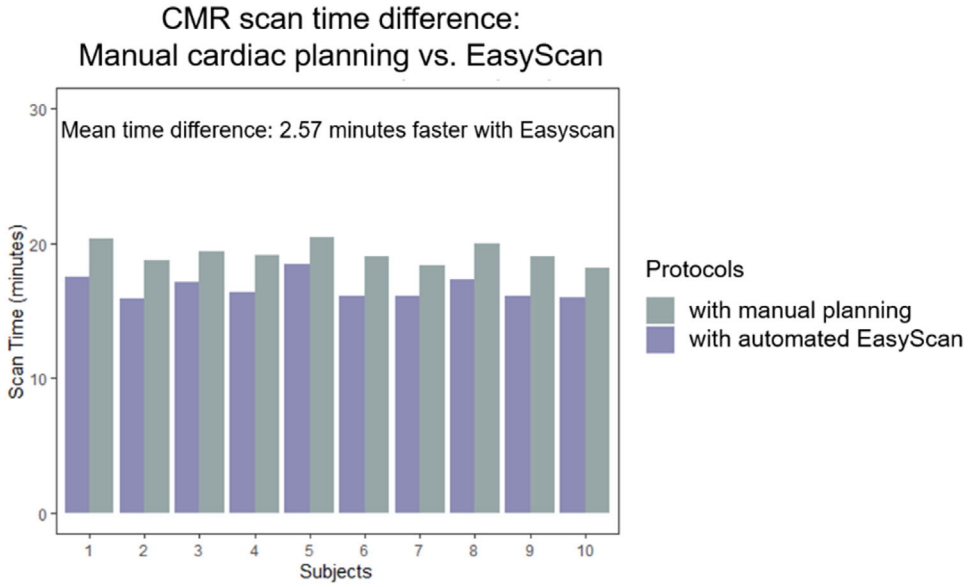

FIGURE 4 MRI protocol acquisition time differences (for 10 healthy subjects) between the two cardiovascular magnetic resonance (CMR) protocols: with manual cardiac planning and with EasyScan planning

(including tissue characterization imaging for single-slice T1 and T2 mapping at the mid-ventricular level). This equated to 13% faster CMR imaging (i.e., 2.57 min, $p < 0.001$, 95% CI [2.31, 2.83]) using the protocol with EasyScan (Figure 4).

3.2.2 | Angular error in cardiac planes

To evaluate the performance of automated cardiac planning using EasyScan, cardiac plane angulations were compared with those manually selected by a highly experienced MR technologist at the time of acquisition (Table 2). Angulations were computed for four cardiac planes obtained from 10 volunteers. For SAX plane, the mean angular error was $6.2 \pm 3.3°$. For long-axis planes the mean angular error for the four-chamber plane was $4.4 \pm 1.4°$; for the two-chamber plane was $5.8 \pm 2.5°$; and for the three-chamber plane was $5.5 \pm 3.5°$. The EasyScan results, including the processing time (0.2 s), are referenced to published strategies.[6,8,11,12,22]

3.3 | Volume shim versus AI-based cardiac shim

3.3.1 | SNR

The output of the AI shim algorithm compared with the standard manual volume shim for two, thrree, four chambers and a mid-ventricular short-axis slice is shown as a distribution representing off-resonance frequency variation (Figure 5). Field map uniformity and frequency profile (in Hz) of an ROI drawn on the septal wall of an example four-chamber view showed that AI shim improved field homogeneity compared with the manual volume shimming (Figure 6). Comparing the SNR of all datasets consisting of healthy and cardio-oncology subjects (Table 3), cine images acquired with AI shim had higher SNR (12.49 %; $p = 0.002$) of the LV myocardium than those obtained with volume shim for all four cardiac orientations: 32.90 ± 7.42 for volume shim and 37.01 ± 8.87 for AI shim. A similar SNR trend was observed between volume and AI shims (13.35% higher SNR with AI shim; $p = 0.019$) for the RV myocardium in the four-chamber and SAX cine views: 29.84 ± 6.73 and 33.82 ± 8.16 for volume and AI shims, respectively. Figure 7 (top row) shows SNR changes within each group (box plots), reflecting higher SNR measurements using AI shim compared to the manual volume shim for cine images at two-, three-, four-chambers, and SAX views. Bland–Altman comparisons of LV/RV measurements for the two shim modes are provided in Figure 8 (left column). SNR changes between volume and AI shims were different ($p < 0.05$) for all cine views except for SNR for RV with SAX view in the patient group ($p = 0.083$).

3.3.2 | CNR

The results of the quantitative CNR analysis of LV and RV myocardium in the healthy and cardio-oncology patient groups are shown in Table 3. LV myocardium CNR was 12.48% higher for cine imaging with AI shim (149.02 ± 39.15) than volume shim (132.49 ± 33.94) across all subjects and for all cardiac planes

TABLE 2 Accuracy of imaging planes (by angular error in degrees) prescribed by EasyScan compared with planes prescribed by the MRI technologist (manual planning) and also compared with previously reported methods

	Angular error (°)				Process time (s)
	SAX	4CH	2CH	3CH	
Volunteer 1	2.8	3.8	4.2	2.4	
Volunteer 2	3.2	3.2	4.5	13.1	
Volunteer 3	11.4	7.2	6.3	5.6	
Volunteer 4	3.8	5.6	6.0	6.7	
Volunteer 5	10.8	5.11	3.2	3.8	
Volunteer 6	2.0	2.9	8.0	2.7	
Volunteer 7	3.4	3.1	3.4	11.0	
Volunteer 8	7.8	2.6	7.2	2.6	
Volunteer 9	9.0	6.2	3.9	3.2	
Volunteer 10	7.3	4.9	11.4	4.1	
Lelieveldt et al.[6]	12.2 ± 6.8	–	–	–	7
Dwivedi et al.[8]	5.6 ± 3.5	–	–	–	240
Lu et al.[11]	8.6 ± 9.7	17.6 ± 19.2	18.9 ± 21.0	12.3 ± 11.0	11
Nitta et al.[12]	3.1 ± 1.7	4.5 ± 3.8	7.3 ± 4.8	5.8 ± 3.8	1.8
Frick et al.[22]	6.7 ± 3.6	7.7 ± 6.1	7.1 ± 3.6	9.1 ± 6.3	–
Our method, EasyScan	6.2 ± 3.3	4.4 ± 1.4	5.8 ± 2.5	5.5 ± 3.5	0.2

Abbreviations: 2CH, two-chamber view; 3CH, three-chamber view; 4CH, four-chamber view; SAX, short axis view.

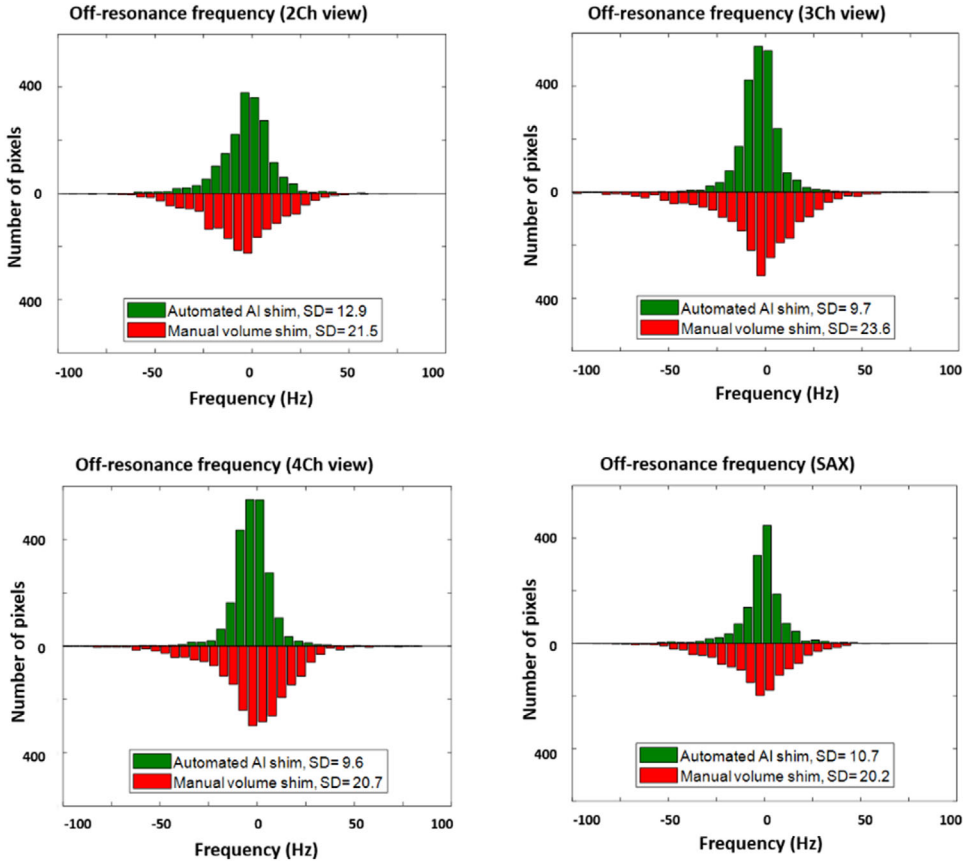

FIGURE 5 The off-resonance distribution of the whole heart mask in the B0 field map obtained from the two shimming methods: manual volume shim versus artificial intelligence (AI) shim. The field map histograms were derived from an identical cardiac mask for both volume shim and AI shim. Histograms were separately generated for each cardiac plane with the standard deviation within the mask region, representing an improved field homogeneity with automated AI shim

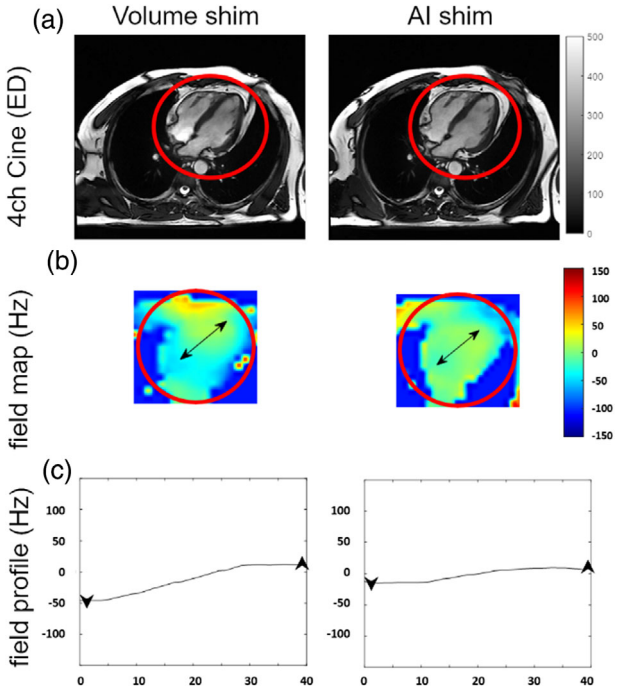

FIGURE 6 An example 4-Chamber cine view of a volunteer at the end-diastolic (ED) phase obtained with manual volume shim and artificial intelligence (AI) shim (a). B0 field map (Hz) distributions limited to heart region showed improved and more uniform field as a result of AI shim application (b). Field profile (in Hz) approximately along the septal wall of myocardium, which is highlighted by a two-way arrow line, where relatively strong field nonuniformity above the septal wall was reduced by AI shimming (c)

($p = 0.004$). The LV CNR analysis of the different cardiac shim methods indicated significant relative CNR increases ($p < 0.05$) with AI shim within each of the two groups (Figure 7, bottom row). Similarly, a 15% CNR increase in the RV myocardium was obtained with AI shim compared to volume shim (AI shim: 168.83 ± 37.58, volume shim: 146.80 ± 30.91; $p = 0.005$). Bland–Altman comparisons between different shims for determining LV and RV CNRs, with associated bias and upper/lower limits of agreements, are presented in the Figure 8 (middle column).

3.3.3 | IQ evaluation

Figure 9 presents four-chamber and SAX cine (mid-ventricular level) image examples from a healthy and cancer patient at the ES phase scanned identically with different cardiac shim methods. Visually, AI shim images were slightly sharper (most notably for the RV free wall) with fewer observed artifacts. The mean sharpness of cine images was 0.64 ± 0.03 for images acquired with volume shim and 0.65 ± 0.03 for those with AI shim, representing 2% sharper images using AI shim ($p = 0.012$). In an analysis of sharpness index measured from cine images acquired with different shims (volume vs. AI), statistical differences were found for healthy subjects (except for three-chamber view; $p = 0.185$) and cardio-oncology patients (except for three-chamber and SAX views). For the IQ assessment, the overall quadratic weighted κ statistics for inter-observer variability showed strong agreement for both SAX cine images with volume shim ($\kappa = 0.74, p < 0.001$) and with AI shim ($\kappa = 0.78, p < 0.001$), where a higher median reviewer score was obtained with AI shim (AI shim: 5 and volume shim: 4, $p = 0.028$) using the five-point rank score method. In correlation analyses, positive correlations were found between observers' scores for IQ for volume shim ($\rho = 0.77, p < 0.001$) and AI shim ($\rho = 0.78$, $p < 0.001$).

3.3.4 | EF

In the healthy group, using the AI shim, the calculated mean LVEF (%) was 64.85 ± 7.04, while that calculated LVEF by the volume shim was 63.04 ± 6.79, with a significant difference ($p = 0.005$, 95% CI = [−2.90, −0.72]). The mean LVEF in the patient group resulted in lower values compared to the healthy group for both shimming methods: LVEF (AI shim) = 50.43 ± 8.42, LVEF (volume shim) = 49.59 ± 8.06, $p = 0.064$, and 95% CI = [−1.75, 0.06]. The mean RVEF of each group of subjects calculated from images obtained with different shim methods are presented in Table 3. RVEF in the healthy group showed no changes between shim methods ($p = 0.053$), while in the patient group, calculated RVEF was different between volume and AI shim ($p = 0.009$). To evaluate the mean and differences of the measured EF from LV and RV myocardium with volume and AI shims, the bland-Altman plots were developed (Figure 8, right column).

3.3.5 | LV absolute wall thickening

The absolute wall thickening of LV myocardium measurement was significantly larger in the healthy group (volume shim: 5.71 ± 1.41 and AI shim: 5.52 ± 1.30) than that in the patient group (volume shim: 3.77 ± 0.86 and AI shim: 4.04 ± 0.92): $p = 0.028$, 95% CI = (0.05, 0.87). Correlations and linear regression analysis between LVEF and absolute LV wall thickening (as determined by volume and AI shims) for the healthy and the patient groups are displayed in Figure 10.

4 | DISCUSSION

Collectively, these results provide evidence that the proposed AI-based techniques (EasyScan and AI shim) benefit CMR imaging with a faster MRI scan protocol and more robust cardiac shimming, while preserving

TABLE 3 Mean values ± standard deviation of measured values for cine scans using volume shim and artificial intelligence (AI) shim

	2CH		3CH		4CH		SAX	
	Volume shim	**AI shim**	**Volume shim**	**AI shim**	**Volume shim**	**AI shim**	**Volume shim**	**AI shim**
Healthy (n = 10)								
Sharpness	0.65 ± 0.02	0.66 ± 0.02^{**a}	0.60 ± 0.02	0.61 ± 0.02	0.64 ± 0.02	0.66 ± 0.02^{***a}	0.66 ± 0.02	0.67 ± 0.01^{**a}
SNR (LV)	30.35 ± 8.45	34.13 ± 10.11^{**a}	32.98 ± 5.80	36.58 ± 4.90^{**a}	33.69 ± 7.21	37.55 ± 8.36^{***a}	35.41 ± 7.19	41.69 ± 9.95^{***a}
CNR (LV)	123.35 ± 34.65	143.20 ± 36.70^{**b}	134.25 ± 22.28	148.23 ± 21.99^{***a}	124.79 ± 18.10	138.47 ± 20.99^{**a}	152.92 ± 28.73	183.29 ± 46.17^{**a}
SNR (RV)	–	–	–	–	31.76 ± 5.45	35.71 ± 6.83^{**a}	27.80 ± 5.59	31.97 ± 7.04^{***a}
CNR (RV)	–	–	–	–	149.46 ± 27.63	174.14 ± 26.37^{***a}	143.67 ± 20.85	169.81 ± 35.40^{**a}
LVEF	–	–	–	–	–	–	63.04 ± 6.79	64.85 ± 7.04^{**a}
RVEF	–	–	–	–	–	–	47.10 ± 8.66	48.16 ± 9.54
absolute left-ventricle (Abs. LV) wall thickening	–	–	–	–	–	–	5.71 ± 1.41	5.52 ± 1.30
Patient (n = 10)								
Sharpness	0.66 ± 0.02	0.67 ± 0.02^{*a}	0.62 ± 0.03	0.63 ± 0.02	0.65 ± 0.01	0.66 ± 0.01^{**b}	0.67 ± 0.02	0.68 ± 0.02
SNR (LV)	28.00 ± 6.69	30.18 ± 8.16^{*b}	33.68 ± 6.14	39.48 ± 7.60^{***a}	36.24 ± 8.09	40.20 ± 8.32^{***a}	32.87 ± 5.39	36.29 ± 6.23^{**b}
CNR (LV)	114.77 ± 40.07	128.59 ± 45.00^{**b}	150.77 ± 42.60	166.60 ± 44.05^{**a}	128.00 ± 24.39	139.89 ± 22.17^{*a}	131.07 ± 31.65	143.91 ± 33.04^{***a}
SNR (RV)	–	–	–	–	33.40 ± 7.88	39.31 ± 8.13^{***a}	26.41 ± 4.60	28.30 ± 5.49
CNR (RV)	–	–	–	–	164.46 ± 35.35	188.42 ± 41.70^{***a}	129.63 ± 25.57	142.94 ± 27.14^{**a}
LVEF	–	–	–	–	–	–	49.59 ± 8.06	50.43 ± 8.42
RVEF	–	–	–	–	–	–	38.63 ± 5.18	39.29 ± 5.34^{**a}
Abs. LV wall thickening	–	–	–	–	–	–	3.77 ± 0.86	4.04 ± 0.92

Note: p values were obtained within each group (volume shim vs. AI shim).
Abbreviations: CNR, contrast to noise ratio; EF, ejection fraction (%); LV, left ventricle; RV, right ventricle; SNR, signal to noise ratio.
Absolute LV wall thickening unit is in (mm).
[a]Assessed with the *t*-test. [b]Assessed with the Wilcoxon signed rank test.
$^{*}p < 0.05$, $^{**}p < 0.01$, $^{***}p < 0.001$.

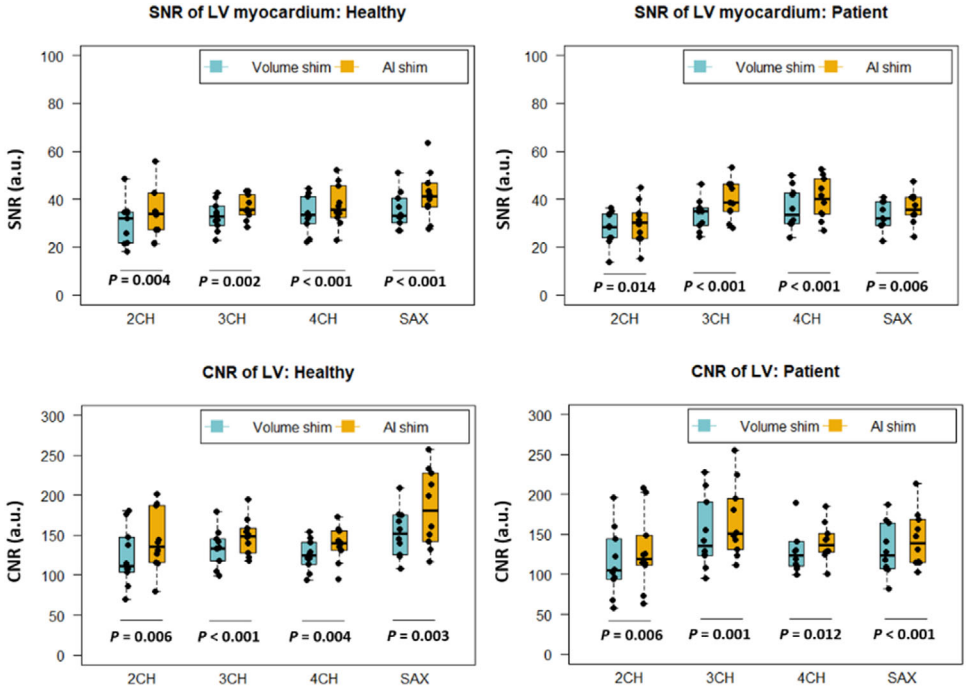

FIGURE 7 Boxplot comparisons of left ventricle (LV) signal-to-noise ratio (SNR) (top row), and contrast-to-noise ratio (CNR) (bottom row) variations for two-, three-, four-chamber and SAX cine views obtained with manual volume shim and artificial intelligence (AI) shim: healthy ($n = 10$) and patient ($n = 10$). The images collected with AI shim showed relatively higher SNR and CNR compared to those obtained with volume shim for all cardiac planes

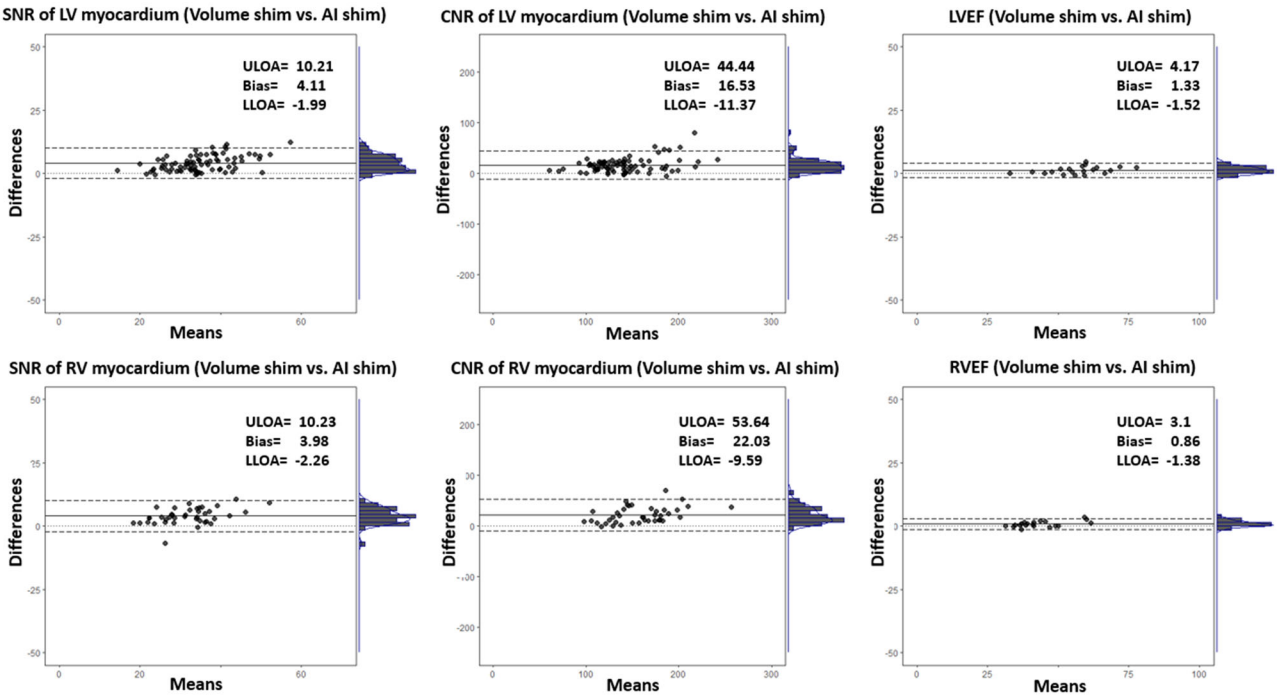

FIGURE 8 Bland-Altman comparisons (with marginal histogram for agreements between volume shim and artificial intelligence [AI] shim) of left ventricle (LV) (top row) and right ventricle (RV) (bottom row) measurements for signal-to-noise ratio (SNR), contrast-to-noise ratio (CNR), and ejection fraction (EF). LV SNR, and CNR measurements derived from four cardiac planes, while RV derived from two planes of four-chamber and SAX cines. The mean of differences is represented by the solid line (bias) with their upper and lower limits of agreement (upper limit of agreement (ULOA) = mean of differences + 1.96 standard deviation and lower limit of agreement (LLOA) = mean of differences − 1.96 standard deviation). Histogram plot of differences between measurement by volume shim and AI shim is also illustrated

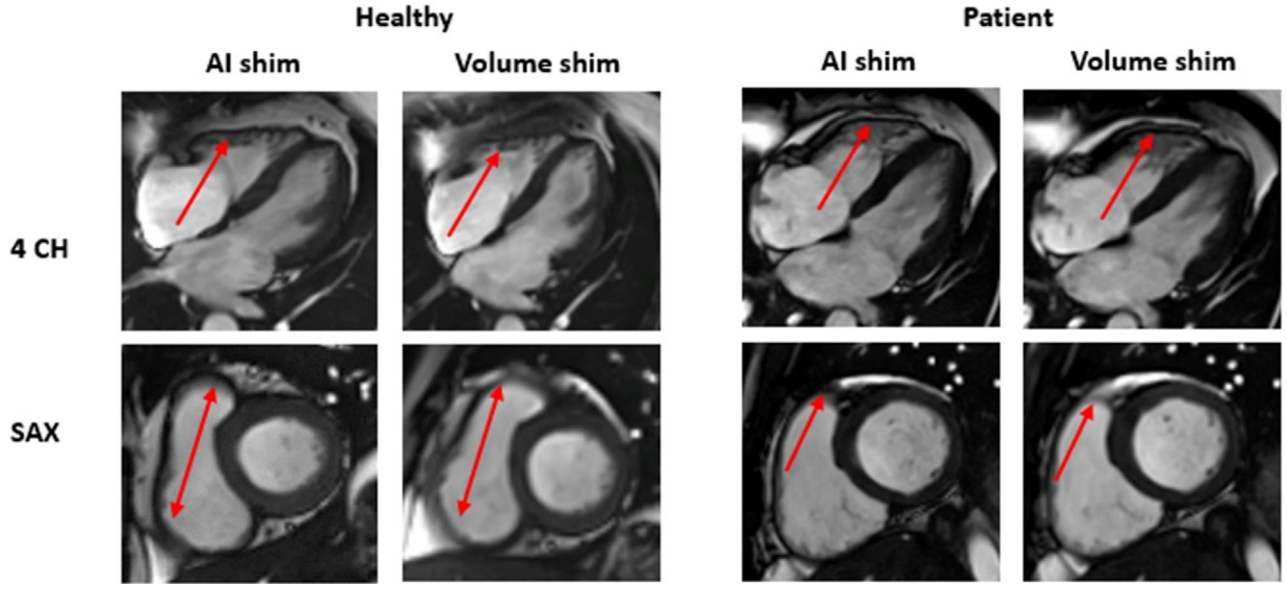

FIGURE 9 Examples of four-chamber and SAX cine images obtained from a healthy and a patient with volume shim and artificial intelligence (AI) shim that shows slightly sharper (less blurry) images with AI shim, especially at the right ventricle (RV) (red arrows) free wall (b)

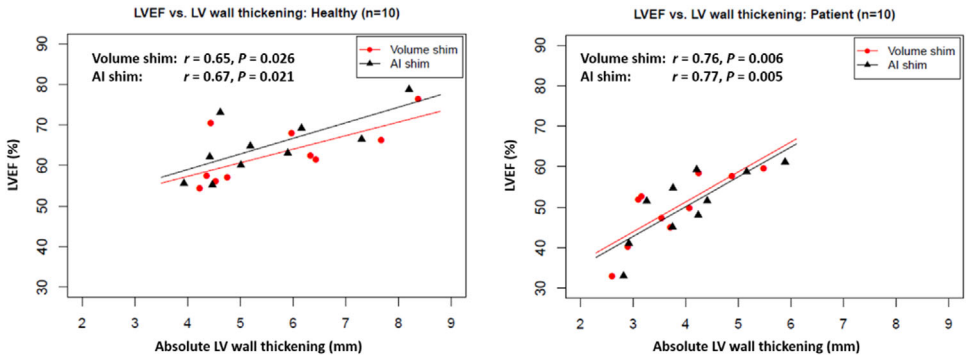

FIGURE 10 Linear regression analysis of correlation between left ventricle ejection fraction (LVEF) and absolute LV wall thickening derived from volume shim and artificial intelligence (AI) shim for healthy subjects and patients. LVEF and absolute LV wall thickening obtained from cine images using AI shim method showed significantly higher Pearson correlation in comparison with volume shim method, where stronger correlation coefficient was found in patients

IQ in routine clinical practice. Compared with manual cardiac planning (requiring four BHs for plane prescriptions, (Figure 1b), EasyScan (single scan with 1 BH, (Figure 1a) minimized operator dependence and reduced overall scanning time by over 2 min (~13% faster, $p < 0.001$). EasyScan simplified cardiac image planning with clinically acceptable planes in all subjects comparable to an expert MRI technologist. Moreover, EasyScan planning had better accuracy, that is, less plane angulation error, than previously reported values[11,22] for all four cardiac views. While, the angular error of Nitta et al.[12] for the long-axis views was similar, EasyScan processing time was nine times faster. Reducing technical demands on MR technologists and shortening total scan time for cardiac patients are important work-flow achievements that will expand and help democratize the use of CMR in both high and low volume institutional settings.

The major limitation of cine bSSFP is the presence of banding artifacts that can be reduced by proper shimming techniques. Lee et al.[23] demonstrated a shim method based on minimization of the maximum off-resonance frequency that improves banding artifact reduction for brain imaging at 3 T. They showed that their shimming method reduced the spatial field inhomogeneity and increased the SNR in bSSFP imaging as well as functional contrast in bSSFP fMRI. In the present study, SNR of cine images was significantly higher in images obtained with AI shim compared with volume shim. Increased SNR with AI shim was evident

across all cine planes for both RV and LV myocardium. For instance, the mean SNR of LV myocardium for the SAX cine with AI shim improved 17.75% ($p < 0.001$) in the healthy and 10.40% ($p = 0.006$) in the patient groups (vs. volume shim). Analogous findings were revealed for CNR measurements between shim methods. Others have reported that increased SNR and contrast between blood and myocardium improve endocardial border definition.[24] Similarly, the elevated SNR and CNR achieved with AI shim facilitated a better delineation of epi- and endocardial borders and consequently, increased the efficiency and accuracy of automated contour detection algorithms utilized by the advanced CMR analysis software available on the scanner.

Image sharpness over all four cardiac planes was slightly increased (2%) by the AI shim. This improvement was most notable at the RV free wall (less blurred) for the four-chamber and short-axis views as illustrated in Figure 9. The subjective IQ assessments also supported the benefit of AI shim versus volume shim. Collectively, the IQ assessments (subjective and objective) suggested that cine images using AI shim were slightly sharper with higher IQ score than those obtained with volume shimming.

CMR imaging with stack short-axis cine acquisition is the gold standard for LVEF measurements because of its volumetric approach for nonsymmetric ventricles with wall motion abnormalities.[25] In the functional CMR analyses, the mean LVEF by AI shim was shown to differ from volume shim in the healthy group ($p = 0.005$) with a relatively small LVEF change between the two methods (2.87% higher with AI shim). As expected, mean LVEF from the patient group was lower than the healthy group with a slight nonsignificant change noted between volume and AI shim methods (1.70% higher with AI shim, $p = 0.064$). Similarly, slightly higher RVEFs were derived from CMR cine images with AI shimming in all subjects (healthy: 2.25%, $p = 0.053$ and patient: 1.71%, $p = 0.009$), which may reflect improved endocardium delineation.

As stated earlier, the LV absolute wall thickening (in mm) showed that differences exist between shim methods for each group with larger changes observed in the patient group (healthy: 3.31%, $p = 0.234$ and patient group: 7.29%, $p = 0.059$). The impact of the absolute LV wall thickening has been previously demonstrated as a sensitive determinant to LVEF in CMR[26] and echocardiography.[27,28] In Rodrigues et al,[26] CMR absolute LV wall thickening showed significantly higher correlation with LVEF in patients with hypertensive heart disease ($r = 0.70, p < 0.001$). This finding was observed in the current study, which showed stronger correlation between absolute LV wall thickening and LVEF in patients than in healthy subjects. Linear regression analysis further demonstrated a stronger correlation coefficient between absolute LV wall thickening and LVEF with AI shim than volume shim ($p < 0.05$).

Although feasibility of the proposed method was demonstrated, this study has limitations. Besides the relatively small sample size, slight shifts occasionally occurred in SAX oriented slices between volume and AI shims image acquisition due to patient movement between scans. This negative effect is likely minimized because covering the entire heart from basal to apical slices (~10 slices) rather than as a single slice reduced the variability of slice locations. Although manual ROI tracing was required, care was taken for consistency across all subjects for SNR and CNR estimations, but the overarching intent is for an operator-independent method to minimize this variability. All scans assessed the complete palette of standard CMR measurements, including myocardial mass and chamber volumes. However, this proof-of-concept study focused on LV wall thickness and EF, which are used extensively by cardiologists adopting societal medical management guidelines. Although the trends of improved IQ likely apply to all myocardial assessments, specific studies addressing the myriad measurements over larger patient cohorts will offer broader technical validation. The independent benefit of AI shim on field inhomogeneities was not considered, but its application showed merit in volunteers and patients with cancer based on quantitative image sharpness and subjective scoring by expert MRI readers. The proof-of-concept benefit of AI shim was appreciated in the small cohort of volunteers and patients in the present study, but assessments with diverse demographic and disease stratification are warranted. Finally, consistent breath-holding position is also important for both EasyScan and AI shim, since both assume that subject position during pre-scan is the same as during later imaging sequences. Although the conventional volume shim workflow also suffers from this problem, AI shim workflow is more sensitive since it aims to optimize the B0 field within the predetermined mask of the heart for cardiac cine.

5 | CONCLUSIONS

Performing CMR exam using AI-based EasyScan for cardiac planning and AI-based shim demonstrated notable improvements compared to a CMR exam with manual cardiac planning and volume shimming. Foremost among these changes was the considerable reduction in scanning time by EasyScan and improved field homogeneity using AI shim. Additionally, the benefits of AI shim to manual volume shim were demonstrated in our studied cohorts. Collectively, the use of AI to achieve a simpler and faster workflow chain will increase institutional availability and quality control by minimizing technical complexity, by shortening scan times, and by improving patient tolerance of CMR studies.

ACKNOWLEDGMENTS

The authors would like to thank Dr. Lingzhi Hu and Jian Xu for their helpful technical advice. Partial funding was provided to the corresponding author by NIH R01 CA216840-01A1 and U54 CA199092.

CONFLICT OF INTEREST

Masoud Edalati, Yuan Zheng, Liu Liu, Shuheng Zhang, and Yanli Song work for the United Imaging Healthcare America (UIHA). Gregory M. Lanza receives instrumentation support through a research collaboration agreement between Washington University Medical School and UIHA. The other authors have no conflict to disclose.

NIH, Grant Numbers: R01 CA216840-01A1 and U54 CA199092

DATA AVAILABILITY STATEMENT

The data that support the findings of this study are available from the corresponding author upon reasonable request.

REFERENCES

1. Hundley WG, Bluemke DA, Finn JP, et al. ACCF/ACR/AHA/NASCI/SCMR 2010 expert consensus document on cardiovascular magnetic resonance: a report of the American College of Cardiology Foundation Task Force on Expert Consensus Documents. *Circulation*. 2010;121(22):2462–2508.
2. Heckbert SR, Post W, Pearson GD, et al. Traditional cardiovascular risk factors in relation to left ventricular mass, volume, and systolic function by cardiac magnetic resonance imaging: the Multiethnic Study of Atherosclerosis. *J Am Coll Cardiol*. 2006;48(11):2285-2292.
3. Kramer CM, Barkhausen J, Flamm SD, Kim RJ, Nagel E, Society for Cardiovascular Magnetic Resonance Board of Trustees Task Force on Standardized Protocols. Standardized cardiovascular magnetic resonance (CMR) protocols 2013 update. *J Cardiovasc Magn Reson*. 2013;15:91.
4. Puntmann VO, Valbuena S, Hinojar R, et al. Society for Cardiovascular Magnetic Resonance (SCMR) expert consensus for CMR imaging endpoints in clinical research: part I - analytical validation and clinical qualification. *J Cardiovasc Magn Reson*. 2018;20(1):67.
5. Lelieveldt BPF, van der Geest RJ, Ramze Rezaee M, Bosch JG, Reiber JHC. Anatomical model matching with fuzzy implicit surfaces for segmentation of thoracic volume scans. *IEEE Trans Med Imaging*. 1999;18:218-230.
6. Lelieveldt BPF, van der Geest RJ, Lamb HJ, Kayser HWM, Reiber JHC. Automated observer-independent acquisition of cardiac short-axis MR images: a pilot study. *Radiology*. 2001;221:537-542.
7. Jackson CE, Robson MD, Francis JM, Noble JA. Automatic planning of the acquisition of cardiac MR images. *Med Image Comput Assist Interv*. 2003;2878:541-548.
8. Dwivedi S, Vaidya V, Mullick R, Foo T, Ho V. Methodology for rapid cardiac axis generation from non-gated cardiac MR images. Paper presented at: Proceedings of the 15th Scientific Meeting, International Society for Magnetic Resonance in Medicine; May 19-25 2007; Berlin.
9. Darrow RD, Vaidya V, Govenkar A, Mullick R, Foo TK. One touch imaging for improved cardiac workflow. Paper presented at: Proceedings of the 16th Scientific Meeting, International Society for Magnetic Resonance in Medicine; May 3-9, 2008; Toronto, ON.
10. Darrow RD, Vaidya V, Mullick R, et al. Ground truth evaluation of one touch cardiac imaging. Paper presented at: Proceedings of the 17th Scientific Meeting, International Society for Magnetic Resonance in Medicine; April 18-24, 2009; Berkeley, CA.
11. Lu X, Jolly MP, Georgescu B, et al. Automatic view planning for cardiac MRI acquisition. *Med Image Comput Comput Assist Interv*. 2011;14(Pt 3):479-486. https://doi.org/10.1007/978-3-642-23626-6_59
12. Nitta S, Takeguchi T, Matsumoto N, et al. Automatic slice alignment method for cardiac magnetic resonance imaging. *Magn Reson Mater Phy*. 2013;26:451-461.
13. Simonetti OP, Ahmad R. Low-field cardiac magnetic resonance imaging: a compelling case for cardiac magnetic resonance's future. *Circ Cardiovasc Imaging*. 2017;10(6):e005446. https://doi.org/10.1161/CIRCIMAGING.117.005446
14. Oshinski JN, Delfino JG, Sharma P, et al. Cardiovascular magnetic resonance at 3.0 T: current state of the art. *J Cardiovasc Magn Reson*. 2010;12(1):55. https://doi.org/10.1186/1532-429X-12-55
15. Milletari F, Navab N, Ahmadi S. V-net: fully convolutional neural networks for volumetric medical image segmentation. Paper presented at: 2016 Fourth International Conference on 3D Vision (3DV); October 25-28, 2016; Stanford, CA.
16. He K, Zhang X, Ren S, Sun J. Deep residual learning for image recognition. Paper presented at: IEEE Conference on Computer Vision and Pattern Recognition (CVPR); June 27-30, 2016; Las Vegas, NV. https://doi.org/10.1109/CVPR.2016.90
17. Song Y, Teng Y, Lyu J, et al. Automatic slice alignment in cardiac magnetic resonance using deep learning. SCMR. 2021 (abstract 944335).
18. Kramer CM, Barkhausen J, Bucciarelli-Ducci C, et al. Standardized cardiovascular magnetic resonance imaging (CMR) protocols: 2020 update. *J Cardiovasc Magn Reson*. 2020;22:17. https://doi.org/10.1186/s12968-020-00607-1
19. Dietrich O, Raya JG, Reeder SB, Reiser MF, Schoenberg SO. Measurement of signal-to-noise ratios in MR images: influence of multichannel coils, parallel imaging, and reconstruction filters. *J Magn Reson Imaging*. 2007;26:375-385.
20. Crete F, Dolmiere T, Ladret P, et al. The blur effect: perception and estimation with a new no-reference perceptual blur metric. Paper presented at: Proceeding of SPIE, Human Vision and Electronic Imaging XII; February 12, 2007; San Jose, CA.
21. Osadebey ME, Pedersen M, Arnold DL, et al. Blind blur assessment of MRI images using parallel multiscale difference of Gaussian filters. *BioMed Eng OnLine*. 2018;17:76. https://doi.org/10.1186/s12938-018-0514-4
22. Frick M, Paetsch I, den Harder C, et al. Fully automatic geometry planning for cardiac MR imaging and reproducibility of functional cardiac parameters. *J Magn Reson Imaging*. 2011;34:457-467. https://doi.org/10.1002/jmri.22626
23. Lee J, Lustig M, Kim DH, Pauly JM. Improved shim method based on the minimization of the maximum off-resonance frequency for balanced steady-state free precession (bSSFP). *Magn Reson Med*. 2009;61(6):1500-1506. https://doi.org/10.1002/mrm.21800
24. Thiele H, Nagel E, Paetsch I, et al. Functional cardiac MR imaging with steady-state free precession (SSFP) significantly improves endocardial border delineation without contrast agents. *J Magn Reson Imaging*. 2001;14(4):362-367. https://doi.org/10.1002/jmri.1195
25. Huttin O, Petit MA, Bozec E, et al. Assessment of left ventricular ejection fraction calculation on long-axis views from cardiac magnetic resonance imaging in patients with acute myocardial infarction. *Medicine (Baltimore)*. 2015;94(43):e1856.
26. Rodrigues JC, Rohan S, Dastidar AG, et al. The relationship between left ventricular wall thickness, myocardial shortening, and ejection fraction in hypertensive heart disease: insights from cardiac magnetic resonance imaging. *J Clin Hypertens (Greenwich)*. 2016;18(11):1119-1127. https://doi.org/10.1111/jch.12849

27. Maciver DH. A new method for quantification of left ventricular systolic function using a corrected ejection fraction. *Eur J Echocardiogr*. 2011;12(3):228-234. https://doi.org/10.1093/ejechocard/jeq185
28. Pellikka PA, She L, Holly TA, et al. Variability in ejection fraction measured by echocardiography, gated single-photon emission computed tomography, and cardiac magnetic resonance in patients with coronary artery disease and left ventricular dysfunction. *JAMA Netw Open*. 2018;1(4):e181456.

How to cite this article: Edalati M, Zheng Y, Watkins MP, et al. Implementation and prospective clinical validation of AI-based planning and shimming techniques in cardiac MRI. *Med. Phys.* 2022;49:129–143. https://doi.org/10.1002/mp.15327